


Cite this: *RSC Adv.*, 2022, 12, 33200

Tb³⁺ and Sm³⁺ co-doped Ca₂La₃(SiO₄)₃F phosphor: synthesis, color regulation, and luminescence properties†

Kun Nie,^{a,b} Ranran Zhou,^a Chi-An Cheng,^c Xiuqiang Duan,^a Ziyao Hu,^a Lefu Mei,^d Haikun Liu,^e Luoxin Wang,^a Hua Wang^a and Xiaoxue Ma^{*a}

The polychromatic phosphor with an apatite structure Ca₂La₃(SiO₄)₃F:0.15Tb³⁺,xSm³⁺ (CLSO:0.15Tb³⁺,xSm³⁺) was synthesized *via* a solid-state route. The phase and morphology of the phosphor has been investigated by means of X-ray diffraction (XRD) and scanning electron microscopy (SEM). The structures of the as-prepared phosphor were verified by means of the Rietveld method. The optical performance was investigated thoroughly and the phosphors could emit multicolor light from short wavelengths to long wavelengths by gradually increasing the doping contents of samarium. All the results support that the energy transfer in CLSO:0.15Tb³⁺,xSm³⁺ contributes to the color tunable property of the phosphor.

Received 21st October 2022
Accepted 8th November 2022

DOI: 10.1039/d2ra06648c

rsc.li/rsc-advances

1. Introduction

Light emitting diodes (LEDs) are considered to represent the fourth generation of light sources in the general lighting industry because of their exceptional and unique qualities.^{1–3} Because LEDs possess attractive colors, a tiny form factor, and ease of construction, they have widespread usage in the decoration and night illumination of cities.^{4–6} Combining phosphors with n-UV chips (350–420 nm) is one approach that LEDs gives practical colors in their light output.^{7–9} In broad terms, the phosphor is made up of activators as well as hosts (there are situations where sensitizers are included).¹⁰ Single-phase multicolor phosphors have seen a lot of advancement in recent years thanks to the realization that they can circumvent certain drawbacks, such as varied light decay times and so on. The ion pair Tb³⁺ → Sm³⁺ has the potential to generate light of several colors and satisfy our needs. Samarium has the potential

to generate red light when used as a phosphor activator, whereas terbium has the potential to emit green light when used as a phosphor sensitizer.^{11–13}

An apatite compound is often selected to serve as the host because of its changeable crystal field environment and its strong chemical stability, which is unaffected by the former. M₁₀(XO₄)₆Y₂ is the chemical formula for the apatite structural compound and M might serve as a monovalent cation – usually an alkali metal – but also a trivalent cation like a lanthanide element, or even a divalent cation like an alkaline earth metal; X denotes S, Ge, Si, and P, among others; Y is most commonly shorthand for the element halogen and the element oxygen, both of which function as channel anions.^{14–16} Compounds of apatite have been the subject of much research in a variety of fields and for several different usages. For instance, Sr₉Gd(PO₄)₅(SiO₄)F₂,¹⁷ Ba₂La₃(SiO₄)₃F,¹⁸ Ba₂La₃(SiO₄)₃Cl,¹⁹ *etc.* Considering that several single-phase multicolor phosphors may be generated *via* the transfer of energy between rare earth ions, structure regulation allows for the production of many variations that may be generated from the crystal structure of apatite, which has the potential to remarkably increase the variety of luminous materials and give other alternatives for the sector of solid-state lighting. However, as far as we are aware, there have been no reports concerning Ca₂La₃(SiO₄)₃F (CLSO) doped with samarium and terbium as of yet.

We generated the Tb³⁺ → Sm³⁺ doped with Ca₂La₃(SiO₄)₃F phosphor that features an apatite structure so that we could examine its structure as well as its luminescence characteristics, particularly the energy transmission. Adjustable phosphors in the colors green, yellow, orange, and red were produced by progressively modifying the doping ratio of rare earth ions. The host material remained unchanged during this process.

^aState Key Laboratory of New Textile Materials & Advanced Processing Technology, Hubei Key Laboratory for New Textile Materials and Applications, School of Materials Science and Engineering, Wuhan Textile University, Wuhan 430200, P. R. China. E-mail: knie@wtu.edu.cn; maxiaoxue2010@126.com

^bKey Laboratory of Testing and Tracing of Rare Earth Products for State Market Regulation, Jiangxi University of Science and Technology, Ganzhou 341000, P. R. China

^cDepartment of Bioengineering, University of California Los Angeles, Los Angeles 90095, California, USA

^dBeijing Key Laboratory of Materials Utilization of Nonmetallic Minerals and Solid Wastes, National Laboratory of Mineral Materials, School of Materials Sciences and Technology, China University of Geosciences, Beijing 100083, P. R. China

^eDepartment of Energy and Chemical Engineering, Dongguan University of Technology, Dongguan 523808, China

† Electronic supplementary information (ESI) available. See DOI: <https://doi.org/10.1039/d2ra06648c>



Moreover, the structure and spectral features of phosphors were evaluated. The database of information on solid-state lighting might benefit from having a better grasp of this single phase and multicolor phosphor, which is significant both on a theoretical level and in terms of its practical application value.

2. Experimental details

2.1 Sample synthesis

CLSO:0.15Tb³⁺,xSm³⁺ phosphors were produced using a traditional solid-state technique at a high temperature. During the experiment, a reducing atmosphere was not used. The chemicals required include analytical grade CaCO₃, SiO₂, and NH₄HF₂, as well as La₂O₃ (99.99%), Tb₄O₇ (99.99%), and Sm₂O₃ (99.99%) with a high purity. On an electronic scale, the chosen compounds were given a weight reading that corresponded to their stoichiometric ratio (0.0001 g accuracy) and had not been treated before and at the time of weighing. Next, all the chemicals were mixed in the same mortar and ground consistently. After that, the homogeneous mixture was placed into a corundum crucible. We subsequently initiated the heating process by placing the crucible that contained the uniform mixture inside a high-temperature tube furnace and the program of the high-temperature furnace needed to ensure that the temperature was kept at 1350 °C for 5 h, before cooling at ambient temperature. The sintered block was ground into powder to facilitate the next structural test and spectral test to fully understand the properties of the phosphor.

2.2 Measurement

2.2.1 Structure and morphology. A D8 advanced X-ray diffractometer, which was operated at 40 kV and 30 mA Cu-K α radiation, was used to obtain the diffraction data ($\lambda = 0.15406$ nm, $2\theta = 10^\circ$ – 80° , Bruker, Germany). To refine the powdered crystal structure based on the XRD data, a step scan was performed, using a step speed of 0.02° per step. The duration that each step spent in residence was three seconds, and the range that could be scanned in 2θ was from 5° to 130° . The crystallographic information file (CIF) was acquired *via* the

process of refinement using Topas 3.0. To examine the microscopic features, a scanning electron microscope (SEM) with model number JSM-6701F manufactured in Japan by Hitachi was used.

2.2.2 Spectra. A Hitachi F-4600 fluorescence spectrophotometer was utilized to measure the luminescence spectra at ambient temperature. This instrument was fitted with a xenon lamp that had a power output of 400 volts and 150 watts. The Edinburgh FS5 fluorescence spectrometer was utilized for the purpose of determining the fluorescence lifetime of the samples.

3. Results and discussions

The crystal structure of the prepared phosphor was evaluated by XRD diffraction technology and the test outcomes are depicted in Fig. 1. The picture is mainly composed of XRD spectra of CLSO:0.15Tb³⁺, CLSO:0.15Tb³⁺,xSm³⁺ ($x = 0.04, 0.12, 0.18, 0.22, 0.32$), CLSO:0.15Sm³⁺ phosphors and a Ba₂La₃(SiO₄)₃F (BLSOF) standard card (ICSD no. 170852) was used as the reference. It can be observed that the number of diffraction peaks, their strength, and their location were compatible with the typical card diffraction pattern and that there were no impurity peaks present. This demonstrates that we were successful in synthesizing phosphors with an apatite structure in the absence of any additional impurities. A single-phase solid solution compound formed when the cations Sm³⁺ and Tb³⁺ were introduced into the lattice *in lieu* of La³⁺.

To get the crystallography information, the structure of the phosphor was improved by the use of the Topas 3.0 program and the initial information for Rietveld refinement refers to the crystal structure BLSOF. The Rietveld structure was refined. For the sake of intuition, the obtained results are visualized in Fig. 2. The calculated strength is imaged as the red solid line, the observed strength is imaged as the blue circle, and the refined Bragg diffraction peak position is imaged as the short blue vertical line. The estimated intensity and the actual intensity were compared, and the resulting difference is depicted as a green solid line in the picture. The outcome of

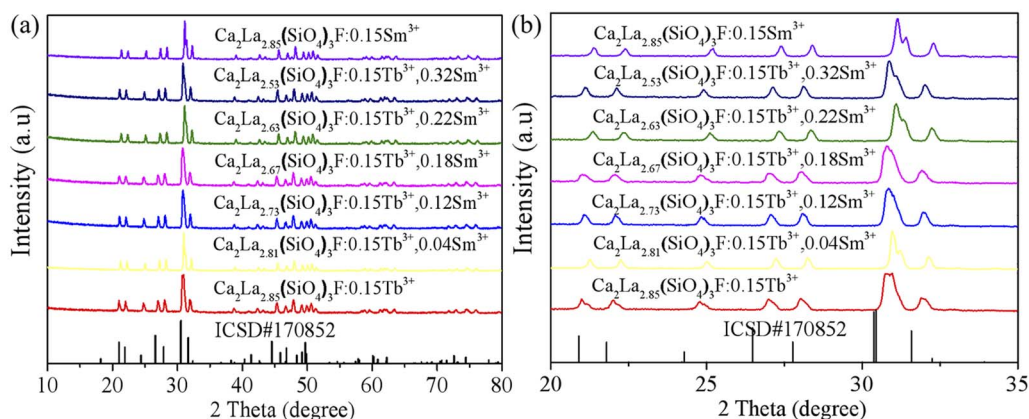


Fig. 1 (a) XRD patterns of CLSO:Tb³⁺,Sm³⁺ samples and (b) the enlarged XRD patterns. At the bottom is the standard card of BLSOF (ICSD no. 170852) for comparison.

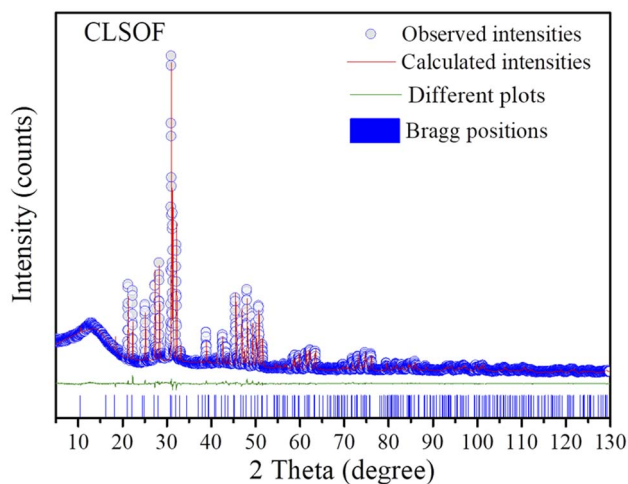


Fig. 2 Rietveld refinement XRD patterns of $\text{Ca}_2\text{La}_3(\text{SiO}_4)_3\text{F}$ at room temperature by TOPAS 3.0 program.

convergence could be reached *via* the process of refining, and lower R factors are depicted in Table 1: $R_{\text{exp}} = 4.586\%$, $R_{\text{wp}} = 7.565\%$, $R_p = 5.297\%$, $\chi^2 = 1.650$. The cell parameters are $a = b = 9.64300(13) \text{ \AA}$, $c = 7.10861(11) \text{ \AA}$ and $V = 572.452(18) \text{ \AA}^3$. The refined atomic coordinates are presented in Table 2 and the isotropic temperature factors for each constituent atom are displayed in CLSOF.

Fig. 3 illustrates the state in the micro world of $\text{CLSOF:0.15Tb}^{3+}, 0.12\text{Sm}^{3+}$. Fig. 3(a) shows the microscopic morphology of the sample, which is irregular and granular. The EDS in Fig. 3(b) depicts the energy spectrum peaks of Ca, La, Si, O, F, Tb, and Sm, which further illustrate the synthesis of the desired samples. The microscopically even distribution of the synthetic sample is demonstrated by the schematic diagram of element distribution that is depicted in Fig. 3(c).

The spectral features of the CLSOF phosphor were examined, especially the excitation and emission spectra. First, the photoluminescence excitation (PLE) and photoluminescence emission (PL) spectra of the CLSOF:0.15Tb^{3+} phosphors were measured and are depicted in Fig. 4(a). This PLE spectrum displayed the normal excitation peaks of Tb^{3+} around 325–

Table 2 Atomic coordinates of CLSOF

Atom	x	y	z	occ	beq
La2	0.24238(28)	0.99034(37)	0.25	0.55	1
Ca2	0.24238(28)	0.99034(37)	0.25	0.45	1
La1	0.6666667	0.3333333	0.98354(51)	0.55	1
Ca1	0.6666667	0.3333333	0.98354(51)	0.45	1
Si1	0.40932(82)	0.36937(75)	0.25	1	1
O1	0.5974	0.4496	0.25	1	1
O2	0.3442	0.4996	0.25	1	1
O3	0.356	0.2721	0.0751	1	1
F	0	0	0.25	1	2.81

500 nm, whereas the emission peak with the strongest intensity was detected at 377 nm ($^7\text{F}_6 \rightarrow ^5\text{D}_3$). The CLSOF:0.15Tb^{3+} phosphor exhibited a strong luminescence when it was activated at a wavelength of 377 nm. Four primary emission peaks made up the emission spectrum: 492 nm ($^5\text{D}_4 \rightarrow ^7\text{F}_6$ transition), 547 nm ($^5\text{D}_4 \rightarrow ^7\text{F}_5$ transition), 592 nm ($^5\text{D}_4 \rightarrow ^7\text{F}_4$ transition), and 624 nm ($^5\text{D}_4 \rightarrow ^7\text{F}_3$ transition), where the one at 547 nm was the strongest.

Second, Fig. 4(b) displays the results of measurements made on the emission and excitation spectra of the CLSOF:0.15Sm^{3+} phosphor. The CLSOF:0.15Sm^{3+} phosphor displayed an intense luminosity when it was stimulated by light with a wavelength of 405 nm. Three primary emission peaks that made up the emission spectrum include 567, 603, and 651 nm with a $^4\text{G}_{5/2} \rightarrow ^6\text{H}_{7/2}$ ($J = 5, 7, 9$) transition. There is some overlap between the PLE (405 nm, 440 nm, and 474 nm) of Sm^{3+} and PL (492 nm) of Tb^{3+} , as can be seen in the portion of the slash that is emphasized in Fig. 4(a) and (b), a theoretical foundation has been provided for the transfer of energy from Tb^{3+} to Sm^{3+} .

Fig. 4(c) depicts the PL and PLE spectra of $\text{CLSOF:0.15Tb}^{3+}, 0.12\text{Sm}^{3+}$ phosphor. Because the only objective of this research was to examine the transmission of energy from Tb^{3+} to Sm^{3+} , it is essential to choose the excitation light of Tb^{3+} to inspire the phosphor. The required PL spectrum was achieved when the phosphor was activated by the PLE spectrum of Tb^{3+} and is illustrated in the purple layer of Fig. 4(c). It should come as no surprise that the emission spectrum was just the superposition of the spectra of samarium and terbium's respective emissions. In the emission spectra that were stimulated by 377 nm, it was possible to locate both the distinctive emission peaks of Sm^{3+} (such as $^4\text{G}_{5/2} \rightarrow ^6\text{H}_{7/2}$ at 603 nm) as well as those of Tb^{3+} (such as $^5\text{D}_4 \rightarrow ^7\text{F}_5$ at 547 nm). This established the groundwork for future studies about the color adjustment of these particular series of phosphors. An energy level diagram with all the relevant transitions is shown in Fig. S1† to visually illustrate the mechanism of luminescence and energy transfer.

As depicted in Fig. 5, the PL spectra of the $\text{CLSOF:0.15Tb}^{3+}, x\text{Sm}^{3+}$ ($x = 0, 0.04, 0.12, 0.14, 0.18, 0.22, 0.24, 0.26, 0.32, 0.34$) phosphors were tested, and Tb^{3+} (at 547 nm) and Sm^{3+} (at 603 nm) have had their signature spectra investigated in great depth. As illustrated in Fig. 5(a), every emission spectrum has the same general shape, but the strength of the peak fluctuates predictably as the amount of Sm^{3+} doping increases. This change is easier to understand and more readily

Table 1 Crystallographic information of CLSOF

Formula	CLSOF
Space group	$P6_3/m$
Symmetry	Hexagonal
a/b (Å)	9.64300(13)
c (Å)	7.10861(11)
a/b	90°
γ	120°
V (Å ³)	572.452(18)
R-Bragg	6.21411374
R_{exp} (%)	4.586
R_{wp} (%)	7.565
R_p (%)	5.297
χ^2	1.650



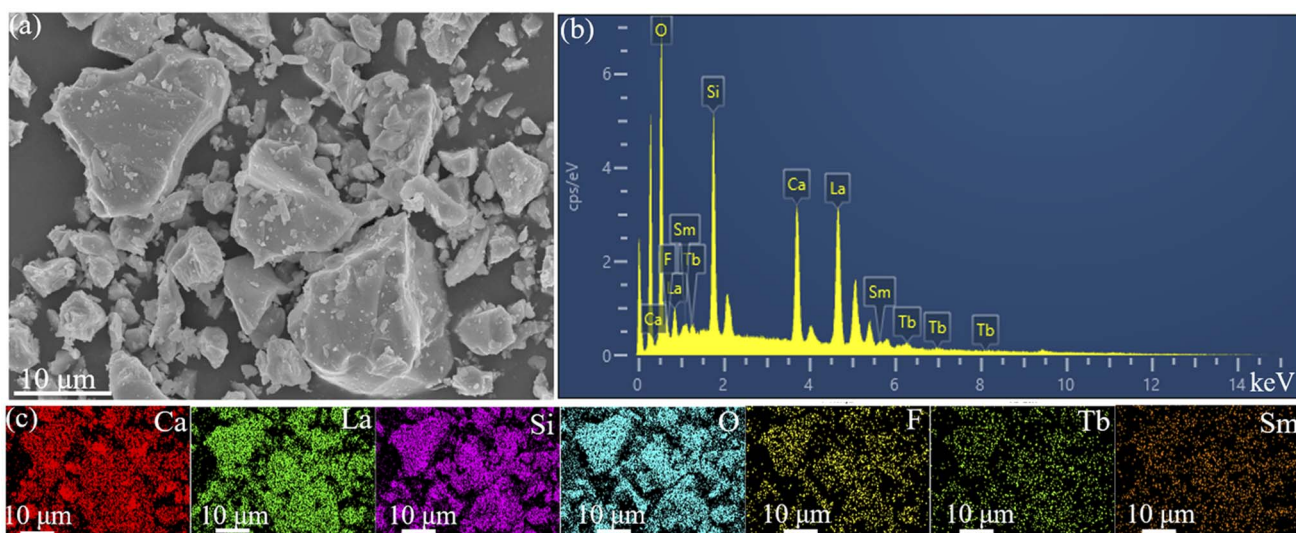


Fig. 3 (a) SEM image, (b) EDS spectrum, and (c) element mapping of CLSOF:0.15Tb³⁺, 0.12Sm³⁺.

apparent in Fig. 5(b): there is a gradual weakening in the peak intensity of Tb³⁺, which may be due to Tb³⁺ transferring its energy to Sm³⁺; in particular, the peak intensity of Sm³⁺ initially

risks, then reaches its highest point at a 0.12 Sm³⁺ doping content, before beginning to weaken, which may be attributed to the fact that Tb³⁺ transfers its own energy to Sm³⁺. These

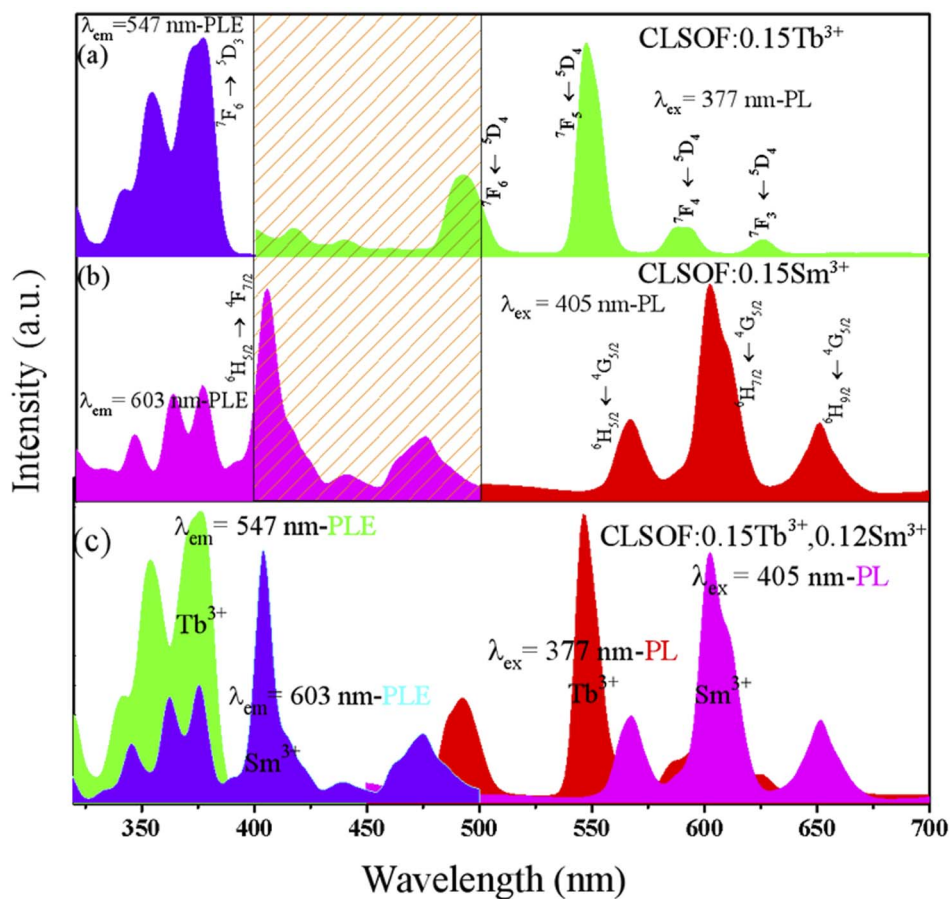


Fig. 4 (a) Photoluminescence excitation spectrum (left) and photoluminescence emission spectrum (right) of CLSOF:0.15Tb³⁺. (b) Photoluminescence excitation spectrum (left) and photoluminescence emission spectrum (right) of CLSOF:0.15Sm³⁺. (c) Photoluminescence excitation spectrum (left) and photoluminescence emission spectrum (right) of CLSOF:0.15Tb³⁺, 0.12Sm³⁺.

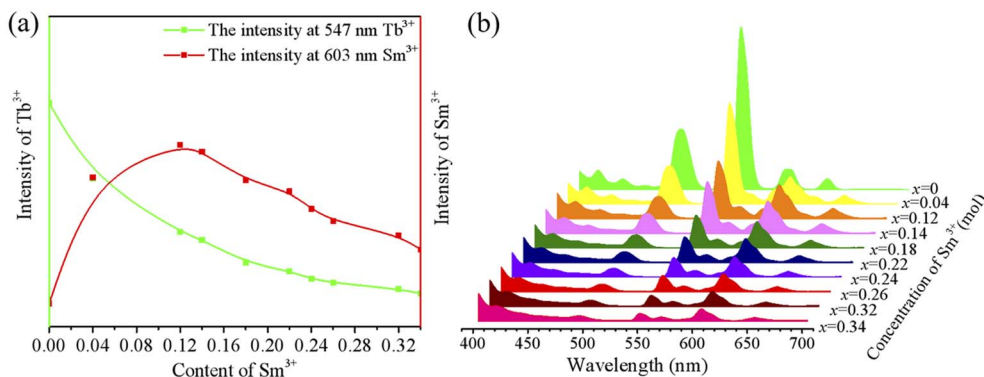


Fig. 5 (a) The PL spectra of the CLSOF:0.15Tb³⁺,xSm³⁺ ($x = 0, 0.04, 0.12, 0.14, 0.18, 0.22, 0.24, 0.26, 0.32, 0.34$) phosphors. (b) The PL intensities of 547 nm (Tb³⁺) and 603 nm (Sm³⁺) when excited by 377 nm with an increase of Sm³⁺ content (x).

experimental observations provide more evidence of the transfer of energy from Tb³⁺ to Sm³⁺. To evaluate the thermal stability of the CLSOF phosphor, we tested the luminous intensity of the phosphor at 298 K, 423 K and 473 K (Fig. S2†), and the luminous intensity retention of the phosphor is shown in Fig. S2†. It can be seen that the phosphor has a good luminous stability when the temperature rises.

To evaluate the mechanism underlying the Tb³⁺ → Sm³⁺ energy transfer, the Tb³⁺ emission lifetime of CLSOF:0.15Tb³⁺,xSm³⁺ which was excited at 377 nm and monitored by 547 nm wavelength were characterized, and the outcomes were consistent with formula (1):^{20,21}

$$I(t) = I_0 + A_1 \exp(-t/\tau_1) + A_2 \exp(-t/\tau_2) \quad (1)$$

In this formula, I denotes the PL intensity at time t , I_0 denotes the intensity at the commencement of the experiment, A_1 and A_2 represent the constants, t denotes the time, whereas τ_1 and τ_2 denote the decay time after the phosphor was subjected to excitation by energy.

According to formula (2), the average lifetime could be acquired by the following formula:^{22,23}

$$\tau^* = (A_1\tau_1^2 + A_2\tau_2^2)/(A_1\tau_1 + A_2\tau_2) \quad (2)$$

Based on the formula, the lifetimes of CLSOF:0.15Tb³⁺,xSm³⁺ are obtained. Obviously, the lifetime of Tb³⁺ is shortened when there is a higher content of Sm³⁺, which further confirmed the transfer of energy that occurred between Tb³⁺ and Sm³⁺ in the CLSOF:0.15Tb³⁺,xSm³⁺.

The efficiency of energy transfer in the CLSOF:0.15Tb³⁺,xSm³⁺ could be acquired by formula (3):^{24,25}

$$\eta = 1 - (\tau_s/\tau_{s0}) \quad (3)$$

Here, τ_{s0} represents the luminescence intensity of the sensitizer Tb³⁺ in the sample in the absence of Sm³⁺, and τ_s represents the luminescence intensity of Tb³⁺ in the presence of Sm³⁺. η denotes the efficiency in energy transfer in CLSOF:0.15Tb³⁺,xSm³⁺ computed as a function of x , as depicted in Fig. 6(b).

When the doping content of samarium in the CLSOF:0.15Tb³⁺,xSm³⁺ is 0.04, 0.12, 0.14, 0.18, 0.22, 0.24, 0.26, 0.32 and 0.34 mol, the energy transfer efficiency is 10.1%, 32.96%, 34.55%, 42.09%, 52.74%, 56.87%, 52.81%, 63.17% and 72.81%, successively, which is visualized in Fig. 7(b). It is obvious that when there is a higher doping content of samarium, a greater efficiency is observed in the transmission of energy.

The non-radiative energy transfer might be caused by either the exchange interaction or the electric dipole interaction between the sensitizer and the activator, or it could be caused between the activator and the activator. The critical distance analysis allows for the classification of the many types of non-radiative energy transmission. According to BLASSE theory, computation of the critical distance R_c may be done using formula (4) as follows:^{26–28}

$$R_c \approx 2(3V/4\pi x_c N)^{1/3} \quad (4)$$

In the formula, V denotes the unit cell volume, x_c denotes the total content of samarium and terbium at an energy efficiency of 0.5, and N denotes the number of cations for one unit cell. In the case of the Ca₂La₃(SiO₄)₃F host, $N = 10$, $V = 572.452 \text{ \AA}^3$. As illustrated in Fig. 7(b), the Sm³⁺ doping content is around 0.3 mol when the energy transfer efficiency is 0.5, so $x_c = 0.21 + 0.15 = 0.36$ mol. Thus, as per the calculation, R_c of CLSOF:0.15Tb³⁺,xSm³⁺ is about 0.6723 nm. Given that the critical distance is higher than 0.5 nm, CLSOF:0.15Tb³⁺,xSm³⁺ utilizes the electric dipole interaction as its mode of energy transfer.

In a general sense, electric dipole interaction may be classified into the following three distinct classifications: dipole–dipole interaction, dipole–quadrupole interaction, and quadrupole–quadrupole interaction. To provide additional evidence on the mode of energy transfer, the following formula (5) was applied:^{29–31}

$$(I_{s0}/I_s) \propto C^{n/3} \quad (5)$$

I_{s0} signifies the PL intensity of Tb³⁺ in CLSOF:0.15Tb³⁺ phosphor, whereas I_s signifies the PL intensity of Tb³⁺ in



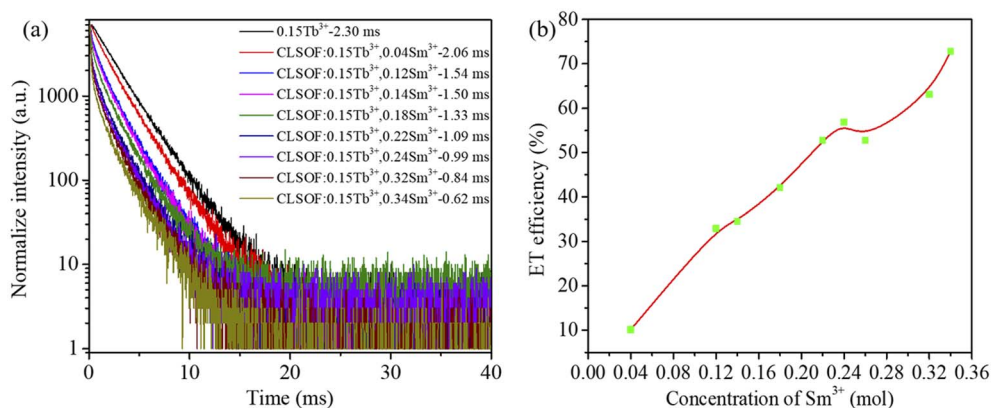


Fig. 6 (a) The fluorescence decay spectra of CLSOF:0.15Tb³⁺,xSm³⁺. The excitation wavelength is 377 nm and the monitor wavelength is 547 nm. (b) The energy transfer efficiency of the phosphor under different contents of Sm³⁺.

CLSOF:0.15Tb³⁺,xSm³⁺ phosphor. C stands for the total samarium and terbium content, and n denotes the constant that may demonstrate the mode of energy transfer between samarium and terbium. The dipole–dipole interaction, the dipole–quadrupole interaction, and the quadrupole–quadrupole interaction are the mechanisms responsible for the transfer of energy when n is 6, 8, and 10, respectively. As portrayed in Fig. 7, when $n = 10$, the linear fitting of I_{50}/I_5 and $C^{n/3}$ ($n = 6, 8$, or 10) produces the optimal results. Therefore, the quadrupole–quadrupole interaction is the mode of energy transfer that underlies CLSOF:0.15Tb³⁺,xSm³⁺.

The color coordinates of the CLSOF:0.15Tb³⁺,xSm³⁺ phosphor were determined premised on the associated emission spectra, and the findings are displayed in Table 3. Additionally, to make the color change of phosphor more obvious, these color coordinates are marked in the CIE diagram (Fig. 8). It is obvious that the color of the phosphor could be changed from green (0.35, 0.62) to yellow and a reddish color (0.47, 0.51) by modifying the ratio of Tb³⁺ to Sm³⁺ in the doping contents. The images displayed from top to bottom in Fig. 8 illustrate the series of phosphors when subjected to irradiation of a 365 nm miner's lamp when the samarium doping level is 0, 0.04, and 0.18 mol of CLSOF:0.15Tb³⁺,xSm³⁺ and CLSOF:0.15Sm³⁺,

Table 3 CIE coordinate values of CLSOF:0.15Tb³⁺,xSm³⁺ at different Sm³⁺ doping contents

Formula	CIE value
Ca ₂ La _{2.85} (SiO ₄) ₃ F:0.15Tb ³⁺	(0.3529,0.6262)
Ca ₂ La _{2.81} (SiO ₄) ₃ F:0.15Tb ³⁺ ,0.04Sm ³⁺	(0.4175,0.5658)
Ca ₂ La _{2.73} (SiO ₄) ₃ F:0.15Tb ³⁺ ,0.12Sm ³⁺	(0.4548,0.5302)
Ca ₂ La _{2.71} (SiO ₄) ₃ F:0.15Tb ³⁺ ,0.14Sm ³⁺	(0.4593,0.5620)
Ca ₂ La _{2.67} (SiO ₄) ₃ F:0.15Tb ³⁺ ,0.18Sm ³⁺	(0.4691,0.5160)
Ca ₂ La _{2.63} (SiO ₄) ₃ F:0.15Tb ³⁺ ,0.22Sm ³⁺	(0.4728,0.5116)
Ca ₂ La _{2.61} (SiO ₄) ₃ F:0.15Tb ³⁺ ,0.24Sm ³⁺	(0.4739,0.5098)
Ca ₂ La _{2.59} (SiO ₄) ₃ F:0.15Sm ³⁺ ,0.26Sm ³⁺	(0.4741,0.5089)
Ca ₂ La _{2.53} (SiO ₄) ₃ F:0.15Tb ³⁺ ,0.32Sm ³⁺	(0.4765,0.5054)
Ca ₂ La _{2.51} (SiO ₄) ₃ F:0.15Tb ³⁺ ,0.34Sm ³⁺	(0.4733,0.5068)
Ca ₂ La _{2.51} (SiO ₄) ₃ F:0.15Sm ³⁺	(0.5648,0.4278)

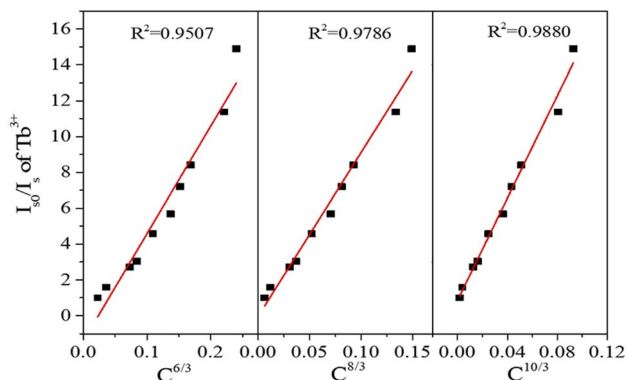


Fig. 7 The relationship between I_{50}/I_5 of Tb³⁺ in CLSOF and $C^{6/3}$, $C^{8/3}$ and $C^{10/3}$.

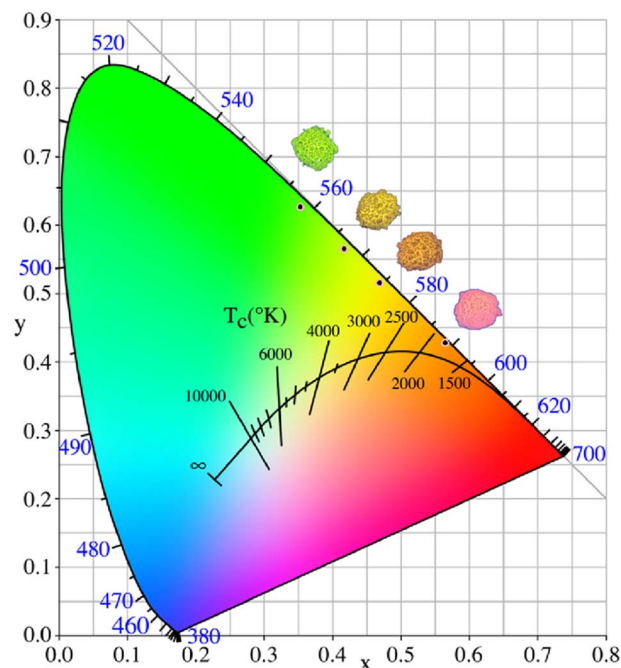


Fig. 8 CIE of CLSOF:0.15Tb³⁺,xSm³⁺ when excited by 377 nm.

respectively. In sum, this set of novel single-phase phosphors, CLSOF:0.15Tb³⁺,xSm³⁺, demonstrates the benefit of configurable polychromatic luminescence due to the transfer of energy.

4. Conclusions

The conventional high-temperature solid phase approach was adopted to produce a single-phase polychromatic phosphor with the formula as follows: CLSOF:0.15Tb³⁺,xSm³⁺. Its structure and optical characteristics have been examined in great depth, and 0.12 mol of Sm³⁺ has been determined to be the optimal content for use in CLSOF:0.15Tb³⁺,xSm³⁺. The quadrupole–quadrupole (q–q) interaction is the mode of energy transmission from Tb³⁺ to Sm³⁺ in CLSOF. The color of the phosphors may be altered from green, yellow/orange, and even reddish color depending on the doping ratio of Tb³⁺/Sm³⁺. All the features acquired above illustrate that CLSOF:0.15Tb³⁺,xSm³⁺ could be one good single-phase multicolor phosphor.

Conflicts of interest

The authors declare no competing financial interest.

Acknowledgements

This research was supported by Key Laboratory of Testing and Tracing of Rare Earth Products for State Market Regulation (Jiangxi University of Science and Technology) (TTRE-P2022YB04), the National Natural Science Foundation of China (51872269, 52274273), the Science and Technology Research Project of Hubei Provincial Department of Education (B2021091), the Key Laboratory for New Textile Materials and Applications of Hubei Province (Wuhan Textile University) (FZXCL202107), the Open Project Program of High-Tech Organic Fibers Key Laboratory of Sichuan Province, China and the National Project Cultivation Plan of Wuhan Textile University. The authors would like to thank Liu Nian and Liu Tianying from Shiyanjia Lab (<https://www.shiyanjia.com>) for the XRD, and SEM characterizations. We sincerely thank Dr Chi-An Cheng of the University of California, Los Angeles, for polishing the paper. This work was partially financially supported by the Guangdong Basic and Applied Basic Research Foundation (2021A1515110283 and 2021A1515110702), the Project funded by China Postdoctoral Science Foundation (2021M702562).

Notes and references

- 1 B. Demir and E. Ayas, *J. Solid State Chem.*, 2022, **306**, 122783.
- 2 K. Nie, X. Ma, P. Lin, N. Kumar, L. Wang and L. Mei, *J. Rare Earths*, 2021, **39**, 1320–1326.
- 3 H. Qian, C. Fan, F. Hussain, K. Song, X. Luo, W. Su, H. Wang, Q. Huang and L. Yang, *J. Lumin.*, 2021, **235**, 117991.
- 4 H. Liu, L. Mei, L. Liao, Y. Zhang, Q. Guo, T. Zhou, Y. Wang and L. Li, *J. Alloys Compd.*, 2019, **770**, 1237–1243.
- 5 B. Demir, D. Derince, T. Dayioglu, L. Koroglu, E. Karacaoglu, V. Uz and E. Ayas, *Ceram. Int.*, 2021, **47**, 34657–34666.
- 6 W. Yan, J. Li, W. Zhang, X. Gao and P. Zhang, *J. Mater. Sci.: Mater. Electron.*, 2021, **32**, 16648–16661.
- 7 P. Dang, G. Li, S. Liang, H. Lian and J. Lin, *J. Mater. Chem. C*, 2019, **7**, 5975–5987.
- 8 H. Liu, L. Liao, S. M. Aksenov, Q. Guo, L. Mei and D. V. Deyneko, *Ceram. Int.*, 2021, **47**, 23300–23308.
- 9 T. Tian, W. Liu, Q. Liu, Y. Zhang, Y. Chu, G. Liu and J. Xu, *J. Rare Earths*, 2022, **40**, 709–716.
- 10 S. Slimi, P. Loiko, K. Bogdanov, A. Volokitina, R. M. Solé, M. Aguiló, F. Díaz, E. Ben Salem and X. Mateos, *J. Alloys Compd.*, 2022, **896**, 163109.
- 11 H.-K. Liu, L.-B. Liao, Y.-Y. Zhang, S. M. Aksenov, N. Liu, Q.-F. Guo, D. V. Deyneko, T.-Y. Wang, L.-F. Mei and C.-H. Sun, *Rare Met.*, 2021, **40**, 3694–3700.
- 12 Y. Wang, G. Lu, Y. Qiu, W. Sun, S. Qin, Y. Lin, B. Deng, D. Zhang and R. Yu, *J. Rare Earths*, 2021, DOI: [10.1016/j.jre.2021.11.006](https://doi.org/10.1016/j.jre.2021.11.006).
- 13 Y. Yuan, H. Lin, J. A. Cao, Q. Guo, F. Xu, L. Liao and L. Mei, *J. Rare Earths*, 2021, **39**, 621–626.
- 14 L. Dong, L. Zhang, Y. Jia, B. Shao, W. Lü, S. Zhao and H. You, *CrystEngComm*, 2019, **21**, 6226–6237.
- 15 Y. Zhang, J. Bin, L. Mei and Z. Huang, *J. Lumin.*, 2019, **206**, 645–648.
- 16 H. Ye, M. He, T. Zhou, Q. Guo, J. Zhang, L. Liao, L. Mei, H. Liu and M. Runowski, *J. Alloys Compd.*, 2018, **757**, 79–86.
- 17 H. Liu, L. Liao, D. Yang, Q. Guo and L. Mei, *Ceram. Int.*, 2016, **42**, 16579–16583.
- 18 X. Ma, L. Liao, Q. Guo, H. Liu, T. Zhou and L. Mei, *RSC Adv.*, 2018, **8**, 27332–27341.
- 19 Q. Guo, X. Ma, L. Liao, H. Liu, D. Yang, N. Liu and L. Mei, *J. Solid State Chem.*, 2019, **280**, 121009.
- 20 Y. Wu, Y. Zhuang, Y. Lv, K. Ruan and R.-J. Xie, *J. Alloys Compd.*, 2019, **781**, 702–709.
- 21 J. Tauc, *Mater. Res. Bull.*, 1968, **3**, 37–46.
- 22 T. M. Tolhurst, T. D. Boyko, P. Pust, N. W. Johnson, W. Schnick and A. Moewes, *Adv. Opt. Mater.*, 2015, **3**, 546–550.
- 23 D. Xu, W. Zhou, Z. Zhang, X. Ma and Z. Xia, *Mater. Res. Bull.*, 2018, **108**, 101–105.
- 24 S. Yan, Y. Jin, D. Pan, G. Xiang, X. Luo and Y. Yang, *Ceram. Int.*, 2018, **44**, 19900–19906.
- 25 P. K. Sahu, M. Ramrakhiani and S. Agrawal, *J. Fluoresc.*, 2019, **29**, 1249–1255.
- 26 X.-X. Ma, W. Zhou, Z. Zhang, X.-R. Wang, B. Zhang and Y.-C. Guo, *J. Lumin.*, 2018, **199**, 82–86.
- 27 Y. Jin, Y. Wang and Y. Wang, *Ceram. Int.*, 2020, **46**, 22927–22933.
- 28 X. Ma, L. Liao, Q. Guo, H. Liu, D. Yang, N. Liu and L. Mei, *RSC Adv.*, 2019, **9**, 35717–35726.
- 29 Y. Zhao, S. Wang, Y.-J. Han, J.-Y. Zhang, C. Liu, X.-F. Hu, Z.-W. Zhang and L.-J. Wang, *J. Lumin.*, 2020, **223**, 117253.
- 30 R. Zhou, C.-A. Cheng, S. Qiu, J. Chen, K. Nie, M. Wu, P. Lin, H. Wang, L. Wang and L. Mei, *RSC Adv.*, 2021, **11**, 28716–28722.
- 31 Y. Ma, X. Peng, M. Fei, W. Zhang, L. Teng, F. Hu, R. Wei and H. Guo, *J. Alloys Compd.*, 2020, **846**, 156435.

